Thermal Actuator Identification and Control for Thermomechanical Real-Time Cyber-Physical Testing

Herta Montoya[1], Manuel Salmeron[2], Christian E. Silva[3], and Shirley J. Dyke[4]

[1]Graduate Research Assistant, Lyles School of Civil Engineering, Purdue University, West Lafayette, IN 47907. Email: montoyah@purdue.edu

[2]Graduate Research Assistant, Lyles School of Civil Engineering, Purdue University, West Lafayette, IN 47907.

[3]Research Scientist, School of Mechanical Engineering, Purdue University, West Lafayette, IN 47907.

[4]Professor, School of Mechanical Engineering and Lyles School of Civil Engineering, Purdue University, West Lafayette, IN 47907.

ABSTRACT

Thermomechanical cyber-physical testing enables two-way thermal coupling between a numerical and an experimental subsystem. The interactions between the numerical model and the physical specimen occur through transfer systems, which enforce interface conditions. Thus, efficient control methodologies are necessary to achieve the desired interface interaction through thermal actuators with minimal error. This study introduces a novel thermal transfer system that imposes distributed cooling (or heating) thermal loads on a physical subsystem. First, the thermal actuator is identified considering switching-mode continuous dynamics for heating and cooling conditions. A switching-mode estimation algorithm is adopted to estimate the operating thermal cycle of the actuator in real-time. A control system is developed to experimentally impose the desired temperature and reduce tracking error (i.e., the error between the desired and actual temperature) under different thermal cycles. The identification and control of the thermal transfer

system are then validated through a set of experiments considering different temperature rates of change. The developed control system is found to effectively minimize tracking errors in real-time cyber-physical experiments.

INTRODUCTION

Cyber-physical testing, or more specifically real-time hybrid simulation (RTHS), is an innovative technology that has transformed engineering experimentation and helped researchers expand modeling capabilities (Gao et al. 2014; Silva et al. 2020). It is a cost-effective technique that supports simultaneous experimental testing and computational modeling to test a system, with the ability to observe any rate-dependent behavior of systems. The interaction between the computational model or counterpart and the physical specimen occurs through transfer systems, which enforce interface conditions. Thus, transfer systems provide the necessary interactions, actuation, and control of actuators to achieve desired objectives.

New and innovative transfer systems must be developed and designed to tackle multi-physics problems and impose appropriate interface conditions, such as distributed loads (Palacio-Betancur and Gutierrez Soto 2023; Najafi et al. 2023). Although advances have been made in cyber-physical testing for the stability and control of mechanical actuators to study the behavior of structures exposed to base motions (Phillips and Spencer 2013; Huang et al. 2019; Condori Uribe et al. 2023), new testing methods have emerged to study thermal effects on structures and systems (Wang et al. 2021; Montoya et al. 2023). Thermal and thermomechanical cyber-physical testing is realized by imposing thermal heat loads on experimental structural elements to evaluate their performance under thermal stresses (Mostafaei 2013; Whyte et al. 2016; Wang et al. 2021). However, the scope of these studies has been restricted to heating thermal loads applied through furnaces and to evaluate changes in the structural responses due to said thermal loads. A novel thermomechanical cyber-physical framework that considers a thermal transfer system's two-way thermal coupling, including cooling or heating, between a numerical and an experimental subsystem was introduced by Montoya et al. (2023). The thermal transfer system consists of the physical equipment (i.e., actuator) and the control methods needed to realize the desired response in the physical specimen.

This novel framework includes a thermal actuator to impose cooling or heating thermal interface conditions through conduction and convection for evaluating the thermal response of the structure, in addition to the mechanical response. The thermal actuator consists of a cryogenic chiller and a "copper-coil cooling plate" design involving a flat plate and fluid coils, often used in liquid cooling systems.

The focus of this paper is on the experimental identification and control of a thermal actuator for thermomechanical real-time cyber-physical testing. The cryogenic chiller exhibits mode-dependent dynamics due to two exchange cycles: heat generation (heating) and consumption (cooling). Herein, a switching-mode controlled dynamic model is proposed and experimentally validated for the cryogenic chiller. Additional thermal actuator components are modeled and experimentally identified through a lumped-capacitance approach. The interacting multiple model (IMM) estimation method is adopted to identify the mode in real-time from measured data to control the switching-mode dynamics of the thermal actuator. The identification and estimation are followed by the development of a control system that accounts for the switching dynamics of the thermal actuator. A switching-mode controller allows the system to perform optimally in both heating and cooling modes by minimizing tracking errors (i.e., the error between the desired and the actual temperature) under different heat cycles. Through a series of experiments, the control methodology for the thermal transfer system is experimentally demonstrated and validated.

THERMAL ACTUATOR DYNAMICS AND EXPERIMENTAL IMPLEMENTATION

In thermomechanical cyber-physical testing, the thermal actuator is an arrangement of individual mechanical components that impose interface thermal conditions between a cyber subsystem and a physical subsystem. These two subsystems are coupled by enforcing temperature and heat flux feedback loops (Montoya et al. 2023). A temperature command is generated for the thermal actuator attached to the physical subsystem (i.e., control plant) to impart a desired temperature. The transient response or dynamics of the thermal actuator must be identified for the successful execution of interface boundary conditions. The experimental implementation and identified dynamics for the thermal actuator are described in this section.

Experimental Setup and Instrumentation

The principal components of the thermal actuator are a cryogenic chiller that uses thermal fluid as the heat transfer medium, a piping system that recirculates the fluid to and from the physical subsystem, and a thermal transfer panel that acts at the boundary of the physical subsystem. The thermal actuator used in this study has a similar design to the temperature control system panel found in Yadav et al. (2021). A schematic diagram of these components is shown in Fig. 1, while photographs of the physical components are shown in Fig. 2(a), (c)-(d).

The *chiller* system can transfer heat to and from an external specimen by adjusting the temperature of a circulating heat transfer fluid (HTF) through a typical thermodynamic loop. The cryogenic chiller used in this study is a MyDax CryoDax 1CD16W.003 water-cooled, refrigerated, recirculating chiller/heater (Mydax Inc.). The circulating HTF used here is Syltherm XLT silicone polymer. The dual heat exchange capacity (i.e., cooling and heating) provided by this fluid enables a broad range of desired temperatures from -70°C to +80°C.

The piping system and thermal transfer panel are the actuator components that transfer heat from the chiller to the physical system. The *thermal transfer pipe system* circulates the HTF supplied by the chiller to the *thermal transfer panel* in contact with the physical subsystem. The transfer panel has a "copper coil cooling plate" design comprised of a flat aluminum plate and a copper coil assembled together through omega-shaped aluminum tracks. The copper coil fixed to the top of the plate circulates the HTF and is in direct contact with omega-shaped tracks to facilitate heat transfer. The thermal transfer pipe system is made of 1-5/8 in copper pipe elements. The thermal transfer panel is made of a 3-mm aluminum plate with a 5/8 in copper coil. Omega-shaped aluminum tracks hold the copper tubing and have complete surface contact when attached to the flat plate.

Open-loop and closed-loop experiments are performed by imposing temperature changes to the thermal actuator components using the MATLAB/Simulink R2020b programming platform (MathWorks), by deploying all the models onto a real-time, high-performance machine manufactured by Speedgoat (Speedgoat). The generated temperature command is transmitted to the internal control logic of the chiller via RS-232 serial communication protocol. Feedback signals are measured by built-in sensors within the chiller, including supply and return HTF temperature and HTF flow rate. The temperature of the piping system and panel is measured with several T-type thermocouples and acquired through thermocouple I/O boards integrated into the real-time performance machine. The thermocouples are carefully located at selected locations of the thermal actuator components and physical subsystems to maximize system observability, with a total of 17 thermocouples. All data measurements are collected at a sampling frequency of 1 Hz, selected based on the slow transient behavior of thermal systems.

Thermal Actuator System Dynamics

This study adopts the thermal actuator dynamics previously described in Montoya et al. (2023). This model is particularly useful for this system as it defines the thermal response for the cryogenic chiller with mode-dependent continuous dynamics. The chiller operates by switching its heat exchange cycles with an internal proprietary and unknown controller. Thus, the dynamics of the controller are included in the plant for identification. Fig. 2(b) shows the open-loop response for the cryogenic chiller that demonstrates the non-symmetric behavior for heat consumption (cooling) and generation (heating). Thus, the chiller is identified and modeled as a linear time-invariant switching system with a switching rule triggered by the continuous state evolution of its output. The dynamic system is represented by the interaction of a discrete signal that switches between individual operation modes and a collection of linear continuous state models that describe each mode. Even though the discrete system mode switches, the output state remains continuous over time.

In the context of this study, the chiller dynamics are defined as the thermal response of the HTF supplied to the point of utilization. The supplied HTF is treated as a lumped-capacitance system with uniform spatial behavior having constant and homogeneous fluid properties. The response is then described with the output HTF temperature T_{C}, such that its temperature rate of change is expressed as

$$\dot{T}_{\mathrm{C}} = -R_{\mathrm{f}}\, T_{\mathrm{C}} + \epsilon\, R_{\mathrm{f}}\, \dot{Q}_{\mathrm{C,capacity}} + R_{\mathrm{f}}\, T_{\mathrm{amb}}, \tag{1}$$

where R_f is the HTF thermal resistance, ϵ is the heat exchange effectiveness coefficient, $\dot{Q}_\mathrm{C,capacity}$ is the heat rate exchange design capacity, and T_amb is the ambient temperature to account for losses to the environment.

The three modes defined for the chiller are OFF, heating, and cooling. The OFF mode describes the behavior when the HTF circulates with no active heat exchanger. The heating mode occurs when the chiller generates and transfers heat to the HTF, while the cooling mode occurs when heat is removed from the HTF. The identified state-dependent switching rule is described by

$$\sigma(T_\mathrm{C}) = \begin{cases} 1: & -e_\mathrm{tol,C} \le T_\mathrm{G,C} - T_\mathrm{C} \le e_\mathrm{tol,C} \\ 2: & T_\mathrm{G,C} - T_\mathrm{C} > e_\mathrm{tol,C} \\ 3: & T_\mathrm{G,C} - T_\mathrm{C} < -e_\mathrm{tol,C} \end{cases} . \tag{2}$$

Here, σ_C is the switching signal or indicator, $e_\mathrm{tol,C}$ is the predetermined internal tracking error tolerance to transition modes, and $T_\mathrm{G,C}$ is the command temperature to the chiller. The OFF, heating, and cooling modes are denoted by values from set $\mathbb{S} = \{1, 2, 3\}$, respectively.

The switching-mode chiller output HTF rate of temperature change, using Eqs. (1)-(2), can be described by

$$\dot{T}_\mathrm{C} = [\mathrm{A}_{\mathrm{C},\sigma}]T_\mathrm{C} + [\mathrm{B}_{\mathrm{C},\sigma}] \begin{Bmatrix} u_\mathrm{C}(\sigma, T_\mathrm{C}) \\ T_\mathrm{amb} \end{Bmatrix}, \tag{3}$$

where $[\mathrm{A}_{\mathrm{C},\sigma}]$ and $[\mathrm{B}_{\mathrm{C},\sigma}]$ are the state and input matrices for switching mode σ, The variable $u_\mathrm{C}(\sigma, T_\mathrm{C})$ is the control mode-conscious input from the chiller defined as

$$u_\mathrm{C}(\sigma, T_\mathrm{C}) = \begin{cases} 0 & : \ \sigma = 1 \\ \dot{Q}_\mathrm{C,heat} & : \ \sigma = 2 \\ \dot{Q}_\mathrm{C,cool} & : \ \sigma = 3 \end{cases} . \tag{4}$$

Here, $\dot{Q}_\mathrm{C,heat}$ and $\dot{Q}_\mathrm{C,cool}$ are the heating and cooling chiller rate design capacity, respectively. The heat rate capacity for the OFF mode is set to 0.

Following the form of Eq. (1), the matrices in Eq. (3) are defined as

$$[\mathrm{A}_{\mathrm{C},1}] = [\mathrm{A}_{\mathrm{C},2}] = [\mathrm{A}_{\mathrm{C},3}] = [-R_{\mathrm{f}}]; \tag{5}$$
$$[\mathrm{B}_{\mathrm{C},1}] = \begin{bmatrix} 0 & R_{\mathrm{f}} \end{bmatrix}; \quad [\mathrm{B}_{\mathrm{C},2}] = \begin{bmatrix} \epsilon_{\mathrm{heat}} R_{\mathrm{f}} & R_{\mathrm{f}} \end{bmatrix}; \quad [\mathrm{B}_{\mathrm{C},3}] = \begin{bmatrix} -\epsilon_{\mathrm{cool}} R_{\mathrm{f}} & R_{\mathrm{f}} \end{bmatrix}.$$

The sign convention regarding the load capacity in cooling mode is negative since heat is being removed from the HTF. For all modes, the output matrix $[\mathrm{C}_\mathrm{C}] = \mathrm{I}_{1\times 1}$ and the feedthrough matrix $[\mathrm{D}_\mathrm{C}] = 0_{1\times 2}$, meaning that the state T_C is directly measurable.

The thermal response for the HTF in the thermal transfer piping system, T_S, is defined as a lumped-capacitance system with input T_C and disturbance T_{amb} due to heat loss. The ultimate form of the rate of change for T_S is given by

$$\dot{T}_\mathrm{S} = -\lambda_{\mathrm{S},1} T_\mathrm{S} + \lambda_{\mathrm{S},2} T_\mathrm{C} + \lambda_{\mathrm{S},3} T_{\mathrm{amb}}. \tag{6}$$

The parameters $\lambda_{\mathrm{S},1-3}$ are lumped representations of the thermal transfer pipe system dynamics that are identified from experimental observations.

Similarly, the thermal transfer panel response is modeled in a lumped-capacitance approach with two heat transfer mechanisms: the HTF loop and contact heat loss (as shown in Fig. 1). The HTF loop represents the heat transfer through fluid motion, and the contact heat loss is the convection heat transfer between the HTF and flat plate. The rate of change for the transfer panel due to the HTF loop, $T_{\mathrm{P,f}}$, and the contact heat loss, $T_{\mathrm{P,l}}$, is described by

$$\begin{Bmatrix} \dot{T}_{\mathrm{P,f}} \\ \dot{T}_{\mathrm{P,l}} \end{Bmatrix} = \begin{bmatrix} -\lambda_{\mathrm{P},1} & 0 \\ 0 & -\lambda_{\mathrm{P},4} \end{bmatrix} \begin{Bmatrix} T_{\mathrm{P,f}} \\ T_{\mathrm{P,l}} \end{Bmatrix} + \begin{bmatrix} \lambda_{\mathrm{P},2} & \lambda_{\mathrm{P},3} \\ \lambda_{\mathrm{P},5} & 0 \end{bmatrix} \begin{Bmatrix} T_\mathrm{S} \\ T_{\mathrm{amb}} \end{Bmatrix}, \tag{7}$$

where $\lambda_{\mathrm{P},1-5}$ are the lumped representations of the thermal transfer panel dynamics when experimentally identified. The thermal transfer output T_P is defined as

$$T_P = w_{P,f}\, T_{P,f} + w_{P,l}\, T_{P,l}\ . \tag{8}$$

The parameters $w_{P,f}$ and $w_{P,l}$ represent the weighting factors associated with each heat transfer process. While the HTF circulates through the thermal transfer panel, the heat loss transfer areas from the initial temperature T_S increase. Consequently, the fluid flowing through the thermal transfer panel experiences a change in temperature from the inlet to the outlet of the HTF loop. The parameters $\lambda_{P,1} - \lambda_{P,3}$ are determined for the sections corresponding to the inlet, middle portion, and outlet areas of the thermal transfer panel.

Further details on the dynamic models and problem formulation for the thermal actuator components are found in Montoya et al. (2023).

Experimental Limitations

Some assumptions are made for the identification of the thermal actuator components. The models adopted assume spatially uniform behavior and rely on fundamental thermal principles constrained by the signals that are measured and accessible. The states that are available for measurement in this study include the temperature and flow rate. The thermal transfer panel model is identified based on three discrete points. Additionally, the HTF is assumed to have constant properties for all heat-exchange cycles and no dependence on pressure (i.e., it is treated as an incompressible fluid). Given the chiller capacity and thermal actuator design, the performance limits of the thermal transfer panel are ~ 2.2°C/min for cooling and ~ 1.0°C/min for heating. Unintentional air gaps that may be present between the panel and the physical system have high thermal resistance, hindering the overall heat transfer capacity.

CONTROL ARCHITECTURE AND METHODOLOGY

Following the switching-mode identification of the thermal actuator, the control architecture for the thermal transfer system is developed to realize the desired temperature in the control plant and reduce tracking errors. The IMM estimation method is adopted to identify the chiller mode from measured available data in real-time, and a switching-mode controller is developed to allow the thermal actuator to perform in each mode with minimal error. Furthermore, a feedback transformation function is introduced to determine the signal used for control tracking from available measurements. The control block diagram for the thermal transfer system is shown in Fig. 3. The estimation, control strategy, and feedback transformation for the thermal transfer system are discussed herein.

Switching-Mode Estimation

The estimation of systems with switching behavior or dynamics can be performed using multiple filter models. The IMM algorithm combines state hypotheses from multiple models to estimate tracking states and determine the matching dynamics with cost-effective computation complexity (Li and Bar-Shalom 1993). The IMM algorithm is adopted here for real-time estimation of the operating heat exchange mode of the thermal actuator. A time-invariant Kalman filter is implemented for each discrete mode of the switched-controlled chiller model with the following form

$$\dot{\widehat{T}}_{\mathrm{C},\sigma} = (\mathrm{A}_{\mathrm{C},\sigma} - \mathrm{L}_{\sigma}\mathrm{C}_{\mathrm{C}})T_{\mathrm{C},\sigma} + \begin{bmatrix}(\mathrm{B}_{\mathrm{C},\sigma} - \mathrm{L}_{\sigma}\mathrm{D}_{\mathrm{C}}) & \mathrm{L}_{\sigma}\end{bmatrix} \begin{Bmatrix} u_{\mathrm{C}}(\sigma, T_{\mathrm{C,m}}) \\ T_{\mathrm{C,m}} \end{Bmatrix}, \tag{9}$$

where $\widehat{T}_{\mathrm{C},\sigma}$ is the continuous chiller output HTF temperature estimate, L_{σ} is the observer gain matrix computing by solving the algebraic Riccati equation, and $T_{\mathrm{C,m}}$ is the measured chiller output HTF temperature.

Fig. 4 shows the structure and flow diagram for the implemented IMM algorithm. The IMM scheme used here is adapted from the algorithm outlined in Bar-Shalom et al. (2001). Before execution, the transition probability matrix of the Markov chain $\pi_{i,j}$ is defined as

$$\pi_{ij} = \begin{bmatrix} p & (1-p)/2 & (1-p)/2 \\ (1-p)/2 & p & (1-p)/2 \\ (1-p)/2 & (1-p)/2 & p \end{bmatrix}, \tag{10}$$

where p is the probability of transitioning from mode $i \in \mathbb{S}$ to mode $j \in \mathbb{S}$. At the same time, the initial mode probability μ is defined equally across the modes as

$$\mu = \begin{bmatrix} 1/3 & 1/3 & 1/3 \end{bmatrix}^{\mathrm{T}}. \tag{11}$$

The initial error covariance matrix, P_j, is projected per mode using the input matrix $\mathrm{B}_{\mathrm{C},\sigma}$ and an estimated process noise covariance Q (Simon 2006)

$$\mathrm{P}_j = \mathrm{B}_{\mathrm{C},\sigma}\mathrm{Q}\mathrm{B}_{\mathrm{C},\sigma}^{\mathrm{T}}. \tag{12}$$

The system is assumed to start from steady-state, and the initial $T_{\mathrm{C},\sigma}$ is the same for all modes. Each Kalman filter j exchanges information with time-varying weights through the IMM algorithm. At the beginning of each cycle, the previous state estimate $\widehat{T_j}$ and error covariance matrix P_j are mixed using computed mode transition probabilities, and new initial conditions for each mode filter are determined. Next, all filters use the measured chiller temperature $T_{\mathrm{C,m}}$ and calculate their respective estimated states and likelihood Λ_j to update the probability of each mode μ_j. Then, the mode-conditioned estimates and covariance of each filter are combined to calculate the final estimated states. Finally, the weights are updated based on which model best fits the data with the estimated mode $\widehat{m}$.

Controller Design

A varying or switching controller is developed for each identified thermal actuator mode. The controller design has three inputs: the setpoint temperature $T_{\mathrm{G,S}}$, the control feedback signal $T_{G,F}$, and the IMM estimated mode $\widehat{m}$. The block diagram for the controller is shown in Fig. 5(a).

The proportional-integral-derivative (PID) algorithm is a common control algorithm for slow transient systems, which is the case in thermomechanical cyber-physical testing. A PID gain bank containing control gains for each thermal actuator mode is generated. The controller gain bank takes the estimated mode $\widehat{m}$ as input, automatically selecting the corresponding mode controller gains that are implemented in the varying PID controller.

If a residual delay is found after the implementation of the PID control, it will require additional compensation. Thus, a feedforward delay compensation layer is added to the control scheme. In this study, the open-loop inverse compensation control developed by Chen and Ricles (2009) is implemented, in which the delay is assumed to be constant over the entire frequency range. The delay compensation block has the form

$$G_{\mathrm{FF}}(z) = \frac{\alpha_d \cdot z - (\alpha_d - 1)}{z}, \tag{13}$$

where α_d is the constant delay compensation.

Feedback Transformation

The scalar controller feedback signal $T_{\mathrm{G,F}}$ is defined to represent the temperature of a surface from a set of available thermocouples, as shown in Fig. 5(b). A feedback measurement transformation uses spatial autocorrelation to determine a representative scalar measurement. It is based on Tobler's first law of geography, which states: "Everything depends on everything else, but near things are more related than distant things" (Tobler 1970).

Assuming that the measurements have spatial dependence and location similarity, one can construct weights that produce a scalar representative value from observations of a variable at different locations. Spatial autocorrelation is based on the interaction of neighboring observations and given a binary contiguity value. Thus, if a sensor measurement shares a border or corner in the observation area with another measurement, it receives a contiguity weight equal to 1. Otherwise, it is assigned a contiguity weight of 0 because it is assumed that there are no similarities.

Assuming all nine thermocouples in Fig. 5(b) are used to determine the feedback signal $T_{\mathrm{G,F}}$, the binary contiguity matrix Υ would be a 9×9 matrix with each column and row representing a sensor. The symmetric matrix Υ represents if there is an interaction between thermocouples with non-zero off-diagonal entries. For example, thermocouple 1 is assigned a contiguity value of 1 with thermocouples 2, 4, and 5 because it either shares a border or corner with the given sensor.

Next, the binary contiguity matrix is normalized to obtain the spatial weights vector υ given by

$$\begin{aligned}\upsilon &= [\mathbf{1}_{1\times 9}\Upsilon]/[\mathbf{1}_{1\times 9}\Upsilon\,\mathbf{1}_{9\times 1}] \\ &= \left\{0.075 \quad 0.125 \quad 0.075 \quad 0.125 \quad 0.200 \quad 0.125 \quad 0.075 \quad 0.125 \quad 0.075\right\}.\end{aligned} \tag{14}$$

The spatial weight factor is higher for thermocouple 5 because it is, by definition, neighbor to all remaining thermocouples. Conversely, thermocouples 1, 3, 7, and 9 have the lowest spatial weight value because of their corner-edge location.

The advantage of using spatial autocorrelation for feedback signal transformation is that it allows the user to obtain a representative signal that is a function of spatial resolution. The number of thermocouples or sensors used for the spatially autocorrelated feedback depends on the test objective or user's preference.

Control Metrics

A set of control metrics is defined to evaluate the tracking performance of the thermal transfer system control. The control metrics are assessed by minimizing error values. The closer these control metric values are to 0, the better the controller performance. The first three control metrics were proposed by Montoya et al. (2023), and defined as

$$J_1 = \sqrt{\frac{\sum_{k=1}^{N}\left(T_{\mathrm{G,F}}[k] - T_{\mathrm{G,S}}[k]\right)^2}{\sum_{k=1}^{N}\left(T_{\mathrm{G,S}}[k]\right)^2}}\,; \tag{15}$$

$$J_2 = \frac{\sqrt{\sum_{k=1}^{N}\left(T_{\mathrm{G,F}}[k] - T_{\mathrm{G,S}}[k]\right)^2/N}}{\max \mid T_{\mathrm{G,S}} \mid}\,; \tag{16}$$

$$J_3 = \frac{\max \mid T_{\mathrm{G,F}} - T_{\mathrm{G,S}} \mid}{\max \mid T_{\mathrm{G,S}} \mid}. \tag{17}$$

where N is the total number of data points.

The first two control metrics are normalized root-mean-square error (NRMSE) measures, while J_3 is the normalized peak absolute error (NPAE).

The integral absolute error (IAE) is introduced as control metric for this study. It is a common control performance index used in optimal control design (Dorf and Bishop 2017; Schultz and Rideout 1961). The IAE integrates the magnitude of the error over time, making it suitable for systems with slow transient and long-term performance, such as a thermal control plant. The IAE is defined as

$$J_4 = IAE = \int_0^{t_f} |T_{\mathrm{G,F}} - T_{\mathrm{G,S}}| \, dt, \tag{18}$$

where t_f is the final time of the evaluation period. The IAE weights all errors equally during the time of evaluation. When comparing controllers, systems with lower IAE values are expected to perform better.

EXPERIMENTAL RESULTS

The experimental dynamics identification and control implementation results for the thermal actuator are described in this section.

Thermal Actuator Identification Results

A set of open-loop experiments with varying command temperatures are performed to identify the parameters and validate the models for the previously discussed thermal actuator dynamics. Table 1 presents the command temperature signals to generate a response from the thermal actuator. For identification, the command signals to the thermal actuator are step functions. The validation experiments consist of a set of step functions and a sine function.

Sensors 2, 5, and 8 (see Fig. 5(b)) are used to identify the parameters of the thermal transfer panel model at the inlet, middle section, and outlet areas. The identified parameters for all thermal actuator components are presented in Table 2. It is worth noting that the pipe configuration in the laboratory, rather than allowing for ambient heat gain, allows for heat loss. Thus, the sign convention for parameter $\lambda_{\mathrm{S},3}$ in Eq. (6) is negative.

To evaluate the identification of the thermal actuator, the NRMSE (same as J_1) is calculated for each component from the validation experiment data sets. On average, the identification NRMSE values for the chiller and thermal transfer pipe system are 3.5% and 2.5%. The thermal transfer panel inlet, middle, and outlet areas have an average NRMSE of 2.5%, 2.9%, and 3.5%, respectively. Figs. 6 and 7 present sample results for the thermal actuator model validation. The results indicate the model dynamics and identified parameters capture the thermal response of the actuator with an NRMSE of less than 5%.

It is important to mention that the switching-mode model determines the plotted discrete chiller mode signal from the chiller output temperature in Figs. 6(d) and 7(d), which is not available experimentally. However, the step signal experiment results in Fig. 6(d) clearly show how the different cycles of the chiller activate to reach the desired command temperature. Opposite to the step signal, the sine function command shown in Fig. 7(d) has changing and lower temperature rates of change. Thus, the control logic results show how the chiller implements the discrete switching control between the heating and cooling cycles with the OFF mode so it does not overcompensate.

The results also indicate the thermal losses through the thermal actuator system components due to the controlled laboratory environment. Thus suggesting the need for a controller to achieve the desired temperature at the thermal transfer panel.

Thermal Control System Experimental Validation

A systematic series of experiments are conducted to validate the developed control approach of the thermal transfer system. Table 3 summarizes the command signals used for control system validation. The type of signal selected for these tests is a sine function with varying temperature rates of change (similar to Signal 10 in Table 1). Tests over the performance limits of the thermal transfer panel are intentionally included to evaluate the controller performance. Tests 1-6 evaluate the control with both cooling and heating cycles, while tests 7-9 only evaluate the cooling cycle controller performance.

PID gains are designed for each of the modes of the thermal actuator. The gains for the OFF mode are P = 1.0, I = 0.009, and D = 75. For the heating mode, the controller gains are P = 0.5, I = 0.01, and D = 75. The controller gains for the cooling mode are P = 1.0, I = 0.01, and D = 75. The delay compensation gain is set to α_d = 120 sec. All nine sensors are used for the feedback transformation. The transition probability for the IMM estimator is set to $p = 0.90$. The process noise covariance Q is modeled as standard normally-distributed Gaussian noise.

The control metrics previously defined are calculated to evaluate the performance of the control system and are provided in Table 3. The time history of representative controlled experiments is shown in Fig. 8. Tests 1-3 results show good control performance supported by low control performance metrics values. Test 4 is slightly over the heating performance limit of the thermal transfer panel and results in a small overshoot at the end of the heating cycle with an increase in the control metric values. Tests 5 and 6 show a larger overshoot and a delay during the heating cycle as $T_{\mathrm{G,S}}$ exceeds the heating performance limit of the thermal transfer panel. The control metrics results for both tests are higher than those within the heating performance limits. However, considering only the cooling mode performance, the control metrics values are much lower, indicating good control performance during the cooling cycle.

Tests 7-9 only consider the cooling, with Tests 8-9 exceeding the cooling performance limit. The results of Tests 7 and 8 suggest good control performance, even when Test 8 exceeds the performance limit of the thermal transfer panel with a small overshoot. Test 9 exceeds by more than 0.5 °C/min the cooling performance limit of the thermal transfer panel, resulting in an overshoot and higher control metric values. It is interesting to note that when the setpoint temperature rate of change is close to the performance limits of the thermal transfer panel, the system will have an overshoot. These overshoots could be further addressed by modifying the controller gains when performing experiments close to or at the performance limits of the thermal transfer panel.

A comparison study with conventional control approaches is performed to further test the proposed switching-mode controller. The switching-mode controller is compared to other control approaches and is denoted herein by SWMC. The first approach considers open-loop conditions, meaning there is no control, denoted by NC. The following three approaches are conventional PID controllers: CCM1 uses the controller gains of the OFF mode, CCM2 uses the controller gains of the heating mode, and CCM3 uses the controller gains of the cooling mode. Additionally, all conventional controllers include delay compensation. The maximum temperature rate of change for comparison is 0.9, within the thermal actuator performance limits.

The results and comparison for all controllers are presented in Fig. 9. The time history and tracking performance results show that controllers CCM2, CCM3, and SWMC have noticeably better performance than controllers NC and CCM1. The control metrics for CCM2 are J_1 = 6.6%, J_2 = 4.1%, and J_3 = 16.1%. For CCM3, the corresponding values are J_1 = 2.7%, J_2 = 1.8%, and J_3 = 3.6%. Controller SWMC has the values of J_1 = 2.8%, J_2 = 1.8%, and J_3 = 5.0%. A comparison of the control metric values suggests that CCM3 and SWMC provide similar performance. However, when comparing the IAE or J_4 in Fig. 9, it is clear that SWMC minimizes the error through the experiment more than CCM3. Additional tests at the heating limits of the thermal transfer panel are performed, and the control metric results show that in such cases, SWMC performs better than CCM3. For example, Test 4 with CCM3 as the controller has the control metric values of J_1 = 16.0%, J_2 = 12.5%, J_3 = 47.5%, and $\arg\max(J_4)$ = 3.93 °C/hour, which are higher than those obtained with controller SWMC provided in Table 3.

Further analysis is done to evaluate the feedback transformation for the controller. All the results thus far considered a feedback transformation using all nine sensor measurements. However, the authors acknowledge that the number of sensors may need to be reduced out of necessity due to high computational requirements as the approach is extended to more complex cases. Thus, we compare the controller performance using a different number of sensors for the feedback transformation. The first scheme considers one feedback measurement using sensor 5, denoted SW1S. The second scheme, denoted by SW3S, considers a spatial distribution transformation using three measurements: sensors 2, 5, and 8. SW9S denotes the spatial transformation using all nine sensor signals. Note this is the nominal case used in the previous validation experiments. Finally, a revised three-measurement scheme using sensors 3, 5, and 7 is denoted as SW3SR.

The results for the controller feedback comparison are shown in Fig. 10. Note that the plotted signals are the representative spatial panel temperature computed using all nine sensors to evaluate if the desired temperature is achieved across the panel. Fig. 10(a) shows how methods SW1S and SW3S are not appropriate to obtain the desired temperature across the panel. Both of these approaches result in delays and the controller not reaching the desired temperature. On the other hand, SW3RS has comparable performance to that obtained using all nine available sensors. It can be seen from Fig. 10(b) that SW3SR can minimize the tracking error in a similar manner as SW9S. These results indicate that using sensors placed closer to the HTF inlet and outlet, plus a middle sensor, provides sufficient feedback information thus allowing the spatial temperature distribution across the panel to achieve the desired setpoint.

CONCLUSIONS

We have presented the experimental identification and controller validation for a thermal actuator implemented for the purpose of thermomechanical cyber-physical testing. The developed and experimentally validated model of a cryogenic chiller as a mode-dependent continuous dynamic system expands thermal cyber-physical testing applications, by imposing cooling or heating loads with minimal tracking error. The model validation results were in good agreement with the experimental response of the thermal actuator, and yielded an NRSME of less than 5% for all components. The thermal transfer system control, estimation, and feedback transformation were discussed and experimentally implemented. The IMM algorithm was adapted and developed to estimate the mode of the thermal actuator in real-time. A switching-mode controller was characterized and evaluated through a set of experiments considering different temperature rates of change, yielding acceptable tracking performance within its design performance range. The developed control design for the thermal transfer system was found to minimize the tracking error more effectively in a physical experiment, in comparison to conventional PID control.

Although the control and identification of the thermal plant were experimentally validated, some limitations of the methodology must be recognized: Identifying the thermal transfer panel as a series of lumped discrete points is sufficient for control purposes. However, when expanding to cyber-physical testing, this approach requires a continuous temperature distribution of the control plant. Thus, a spatial identification of the thermal transfer panel must be performed. Improving the modeling and analysis of the temperature distribution is planned as future work. Additionally, the controller for the thermal actuator results in an overshoot when performing at or over the heat transfer performance limits. Even though these are outside of the intended range of operation, potential methods to prevent this problem can improve the tracking performance of the control method.

DATA AVAILABILITY STATEMENT

Some or all data, models, or code that support the findings of this study are available from the corresponding author upon reasonable request.

ACKNOWLEDGMENTS

This work was supported by the Space Technology Research Institutes grant number 80NSSC19K1076 from NASA's Space Technology Research Grants Program.

REFERENCES

Bar-Shalom, Y., Ling, X. R., and Kirubarajan, T. (2001). "Adaptive Estimation and Maneuvering Targets." *Estimation with Applications to Tracking and Navigation*, John Wiley Sons, Ltd, New York, Chapter 11, 421–490.

Chen, C. and Ricles, J. M. (2009). "Analysis of actuator delay compensation methods for real-time testing." *Engineering Structures*, 31(11), 2643–2655.

Condori Uribe, J., Salmeron, M., Patino, E., Montoya, H., Dyke, S. J., Silva, C., Maghareh, A., Najarian, M., and Montoya, A. (2023). "Experimental Benchmark Control Problem for Multi-axial Real-time Hybrid Simulation." *Frontiers in Built Environment*, 9.

Dorf, R. C. and Bishop, R. H. (2017). "The Design of Feedback Control Systems." *Modern Control Systems*, Pearson Education, Inc., Hoboken, New Jersey, Chapter 10, 700–783.

Gao, X., Castaneda, N., and Dyke, S. J. (2014). "Experimental Validation of a Generalized Procedure for MDOF Real-Time Hybrid Simulation." *Journal of Engineering Mechanics*, 140(4), 04013006.

Huang, L., Chen, C., Guo, T., and Chen, M. (2019). "Stability Analysis of Real-Time Hybrid Simulation for Time-Varying Actuator Delay Using the Lyapunov-Krasovskii Functional Approach." *Journal of Engineering Mechanics*, 145(1), 1–15.

Li, X. and Bar-Shalom, Y. (1993). “Performance prediction of the interacting multiple model algorithm.” *IEEE Transactions on Aerospace and Electronic Systems*, 29(3), 755–771.

MathWorks (2020). *MATLAB version 2020b*, <https://www.mathworks.com/products/matlab.htm>.

Montoya, H., Dyke, S. J., Silva, C. E., Maghareh, A., Park, J., and Ziviani, D. (2023). “Thermo-mechanical Real-Time Hybrid Simulation: Conceptual Framework and Control Requirements.” *AIAA Journal*, 61(6), 2627–2639.

Mostafaei, H. (2013). “Hybrid fire testing for assessing performance of structures in fire—Methodology.” *Fire Safety Journal*, 58, 170–179.

Mydax Inc. (2019). *CryoDax 16 Water-Cooled Chiller/Heater User’s Manual*.

Najafi, A., Fermandois, G. A., Dyke, S. J., and Spencer, B. F. (2023). “Hybrid simulation with multiple actuators: A state-of-the-art review.” *Engineering Structures*, 276(December 2022), 115284.

Palacio-Betancur, A. and Gutierrez Soto, M. (2023). “Recent Advances in Computational Methodologies for Real-Time Hybrid Simulation of Engineering Structures.” *Archives of Computational Methods in Engineering*, 30(3), 1637–1662.

Phillips, B. M. and Spencer, B. F. (2013). “Model-Based Multiactuator Control for Real-Time Hybrid Simulation.” *Journal of Engineering Mechanics*, 139(2), 219–228.

Schultz, W. C. and Rideout, V. C. (1961). “Control system performance measures: Past, present, and future.” *Ire Transactions on Automatic Control*, 22–35.

Silva, C. E., Gomez, D., Maghareh, A., Dyke, S. J., and Spencer, B. F. (2020). “Benchmark control problem for real-time hybrid simulation.” *Mechanical Systems and Signal Processing*, 135, 106381.

Simon, D. (2006). *Optimal state estimation: Kalman, H infinity, and nonlinear approaches*. John Wiley & Sons.

Speedgoat (2020). *Performance Real-Time Machine*, <https://www.speedgoat.com/products-services/real-time-target-machines/performance-real-time-target-machine>.

Tobler, W. R. (1970). “A Computer Movie Simulating Urban Growth in the Detroit Region.”

Economic Geography, 46(332), 234.

Wang, X., Ahn, J.-K., Kwon, O.-S., Kim, R. E., and Yeo, I. (2021). "Development of Temperature and Constraint-Dependent Column Demand-Capacity Curves and Their Validation through Hybrid Fire Simulations." *Journal of Structural Engineering*, 147(4), 1–15.

Whyte, C. A., Mackie, K. R., and Stojadinovic, B. (2016). "Hybrid Simulation of Thermomechanical Structural Response." *Journal of Structural Engineering*, 142(2), 04015107.

Yadav, S., Dhillon, P., Kurtulus, O., Baxter, C., Ziviani, D., Horton, W. T., Karava, P., and Braun, J. E. (2021). "Design and Development of a Human Building Interaction Laboratory." *International High Performance Buildings Conference*, West Lafayette, IN, Paper 362, <https://docs.lib.purdue.edu/ihpbc/362>.

List of Tables

1 Signals for the thermal actuator identification and validation tests. 22

2 Identified thermal actuator system parameters. 23

3 Signals and results of the experimental thermal transfer system control validation. . . 24

TABLE 1. Signals for the thermal actuator identification and validation tests.

Signal #	Input Type	Mathematical Description for Input Signal	A [°C]	t_1 [min]	t_2 [min]	F [Hz]	T_0 [°C]	T_{amb}* [°C]	Process
1,2	Step		0	10	60	-	20	20.5	Identification
3,4	Step		10	10	60	-	20	20.7	Identification
5,6	Step	$T_{\mathrm{G,C}} = \begin{cases} T_0 & t < t_1 \\ -A & t_1 \leq t < t_2 \\ T_0 & t_2 \leq t \end{cases}$	20	10	60	-	20	20.8	Validation
7,8	Step		30	10	60	-	20	20.9	Validation
9	Step		40	10	60	-	20	20.9	Validation
10	Sine	$T_{\mathrm{G,C}} = \begin{cases} T_0 & t < t_1 \\ A(\sin(2\pi F[t - t_1] + \frac{\pi}{2}) - 1) + T_0 & t_1 \leq t < 6t_1 \\ -2A + T_0 & 6t_1 \leq t_2 \\ A(\sin(2\pi F[t - t_2] + \frac{3\pi}{2}) - 1) + T_0 & t_2 \leq t < t_2 + 5t_1 \\ T_0 & t_2 + 5t_1 \leq t \end{cases}$	15	10	72	1/6000	20	20.7	Validation

* T_{amb} is the mean measured ambient temperature at the laboratory during experiments.

TABLE 2. Identified thermal actuator system parameters.

Actuator Component	**Parameter**	**Units**	**Value**	**Description**
Heat Transfer Fluid (HTF)	R_{f}	$\mathrm{K{\cdot}W^{-1}}$	4×10^{-4}	Thermal resistance
Cryogenic Chiller	$\dot{Q}_{\mathrm{C,heat}}$	W	3000	Heating exchange rate design capacity
	$Q_{\mathrm{C,cool}}$	W	7200	Cooling exchange rate design capacity
	ϵ_{heat}	-	0.0123	Heating exchange effectiveness coefficient
	ϵ_{cool}	-	0.0260	Cooling exchange effectiveness coefficient
	e_{tol}	°C	0.25	Internal tracking error tolerance
Thermal Transfer Pipe System	$\lambda_{\mathrm{S},1}$	1/sec	1.4×10^{-2}	State lumped parameter
	$\lambda_{\mathrm{S},2}$	1/sec	1.5×10^{-2}	Input lumped parameter
	$\lambda_{\mathrm{S},3}$	1/sec	8.0×10^{-4}	Disturbance lumped parameter
Thermal Transfer Panel	$\lambda_{\mathrm{P,1,in}}$	1/sec	1.0×10^{-2}	Inlet HTF state lumped parameter
	$\lambda_{\mathrm{P,2,in}}$	1/sec	1.0×10^{-2}	Inlet HTF input lumped parameter
	$\lambda_{\mathrm{P,3,in}}$	1/sec	1.9×10^{-3}	Inlet HTF disturbance lumped parameter
	$\lambda_{\mathrm{P,4,in}}$	1/sec	4.5×10^{-4}	Inlet contact heat loss state lumped parameter
	$\lambda_{\mathrm{P,5,in}}$	1/sec	2.5×10^{-4}	Inlet contact heat loss input lumped parameter
	$\lambda_{\mathrm{P,1,mid}}$	1/sec	1.0×10^{-2}	Mid-panel HTF state lumped parameter
	$\lambda_{\mathrm{P,2,mid}}$	1/sec	9.5×10^{-3}	Mid-panel HTF input lumped parameter
	$\lambda_{\mathrm{P,3,mid}}$	1/sec	2.0×10^{-3}	Mid-panel HTF disturbance lumped parameter
	$\lambda_{\mathrm{P,4,mid}}$	1/sec	6.0×10^{-4}	Mid-panel contact heat loss state lumped parameter
	$\lambda_{\mathrm{P,5,mid}}$	1/sec	4.0×10^{-4}	Mid-panel contact heat loss input lumped parameter
	$\lambda_{\mathrm{P,1,out}}$	1/sec	7.0×10^{-3}	Outlet HTF state lumped parameter
	$\lambda_{\mathrm{P,2,out}}$	1/sec	6.0×10^{-3}	Outlet HTF input lumped parameter
	$\lambda_{\mathrm{P,3,out}}$	1/sec	2.0×10^{-3}	Outlet HTF disturbance lumped parameter
	$\lambda_{\mathrm{P,4,out}}$	1/sec	5.0×10^{-4}	Outlet contact heat loss state lumped parameter
	$\lambda_{\mathrm{P,5,out}}$	1/sec	3.5×10^{-4}	Outlet contact heat loss input lumped parameter
	$w_{\mathrm{P,f}}$	-	0.7	HTF loop weighting factor
	$w_{\mathrm{P,l}}$	-	0.3	Contact heat loss weighting factor

TABLE 3. Signals and results of the experimental thermal transfer system control validation.

Test	Signal									Control Metric Results			
	Type	Cycle	A [°C]	t_1 [min]	t_2 [min]	F [Hz]	T_0 [°C]	T_{amb}* [°C]	Max ROC [°C/min]	J_1 [%]	J_2 [%]	J_3 [%]	max(J_4) [°C/hour]
1	Sine	C&H	2.5	10	48	1/3600	20	20.5	0.25	0.8	0.7	1.6	0.16
2	Sine	C&H	7.5	10	68	1/5500	20	20.6	0.50	1.3	0.9	3.0	0.30
3	Sine	C&H	10	10	62	1/5000	20	20.5	0.75	2.7	1.8	3.6	0.60
4	Sine	C&H	15	10	68	1/5500	20	20.1	1.00	4.8	3.2	9.8	1.10
5	Sine	C&H	20	10	72	1/6000	20	20.2	1.25	16.5 (3.6†)	13.2 (2.9†)	32.7 (6.8†)	4.00 (0.60†)
6	Sine	C&H	20	10	62	1/5000	20	21.2	1.50	20.4 (2.8†)	16.7 (2.3†)	44.1 (5.2†)	4.50 (0.38†)
7	Sine	C	20	10	48	1/3600	20	20.7	2.0	4.2	3.6	6.6	0.61
8	Sine	C	20	10	42	1/3000	20	21.2	2.5	4.0	3.5	6.9	0.50
9	Sine	C	20	10	36	1/2500	20	20.8	3.0	9.1	8.0	16.2	0.98

Note: C and H denote cooling and heating. ROC stands for rate of change.

* T_{amb} is the mean measured ambient temperature at the laboratory during experiments.

† Only cooling cycle considered.

List of Figures

1 Schematic block diagram of the thermomechanical cyber-physical control plant. . . 26

2 Thermal actuator components: (a) cryogenic chiller; (b) cryogenic chiller experimental response; (b) part of the thermal transfer pipe system; and (d) thermal transfer panel. 27

3 Thermal transfer system control block diagram. 28

4 Thermal transfer system IMM algorithm: (a) structure and (b) flow diagram. 29

5 Thermal transfer system components: (a) Controller block diagram, and; (b) thermal transfer panel feedback sensor layout. 30

6 Sample model validation test results (signal 4): (a) chiller; (b) thermal transfer pipe system; (c) thermal transfer in-panel area; (d) chiller mode determined by the model's control logic; (e) thermal transfer mid-panel area; (f) thermal transfer out-panel area. 31

7 Sample model validation test results (signal 10): (a) chiller; (b) thermal transfer pipe system; (c) thermal transfer in-panel area; (d) chiller mode determined by the model's control logic; (e) thermal transfer mid-panel area; (f) thermal transfer out-panel area. 32

8 Thermal transfer system control validation results: (a) Test 1; (b) Test 2; (c) Test 3; (d) Test 4; (e) Test 5; (f) Test 6; (g) Test 7; (h) Test 8; and (i) Test 10. 33

9 Switching-mode controller comparison to other controllers: (a) time history; (b) tracking performance; and (c) IAE error. 34

10 Thermal transfer panel spatial temperature comparison by controller feedback scheme: (a) time history; and (b) IAE error. 35

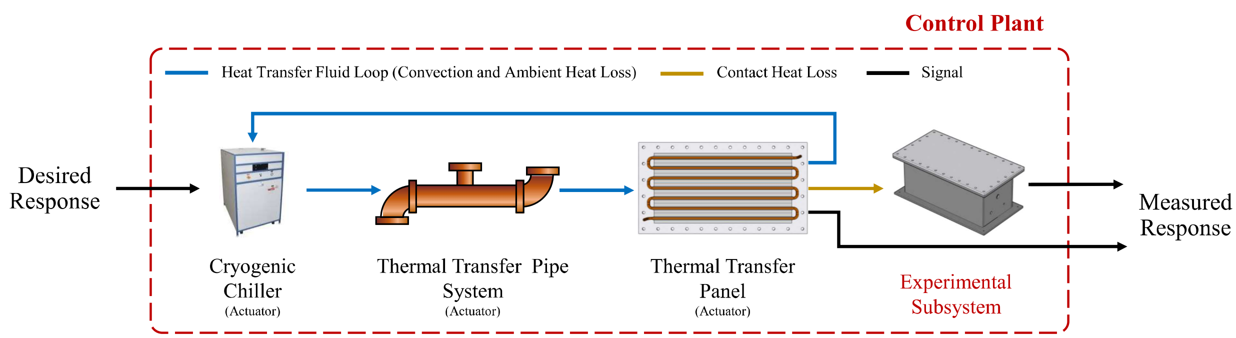

Fig. 1. Schematic block diagram of the thermomechanical cyber-physical control plant.

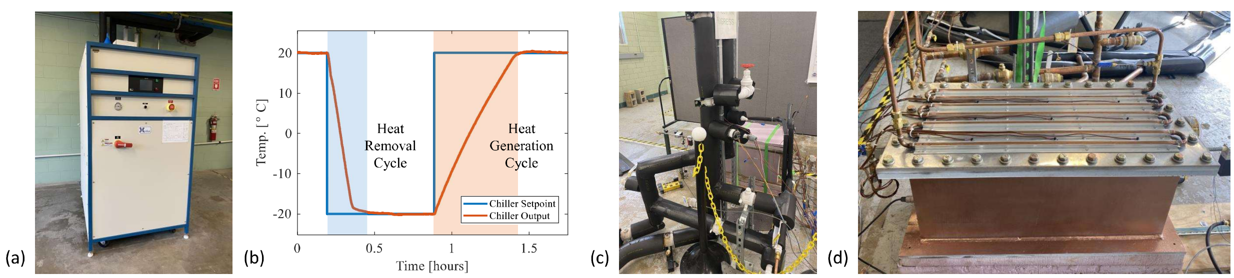

Fig. 2. Thermal actuator components: (a) cryogenic chiller; (b) cryogenic chiller experimental response; (b) part of the thermal transfer pipe system; and (d) thermal transfer panel.

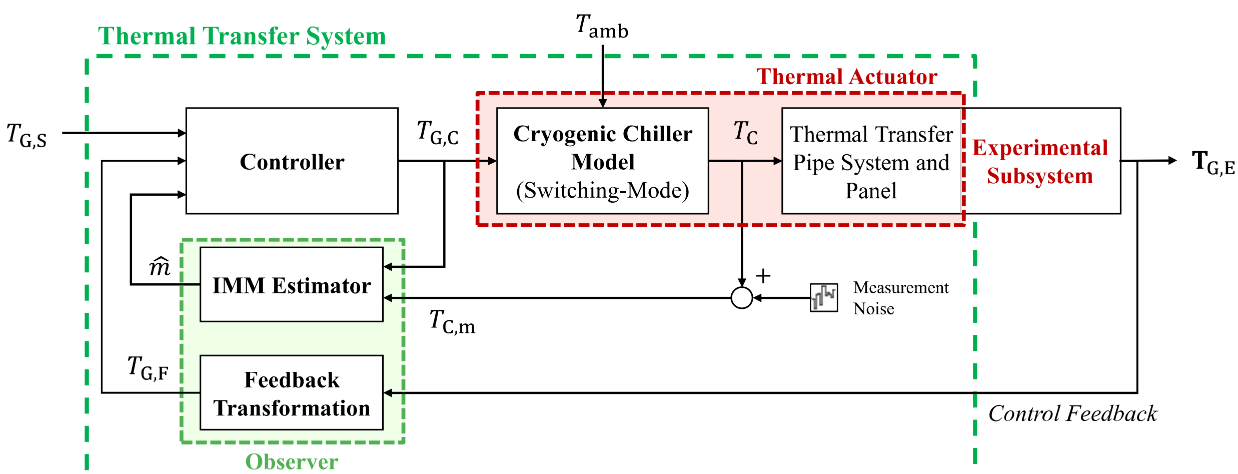

Fig. 3. Thermal transfer system control block diagram.

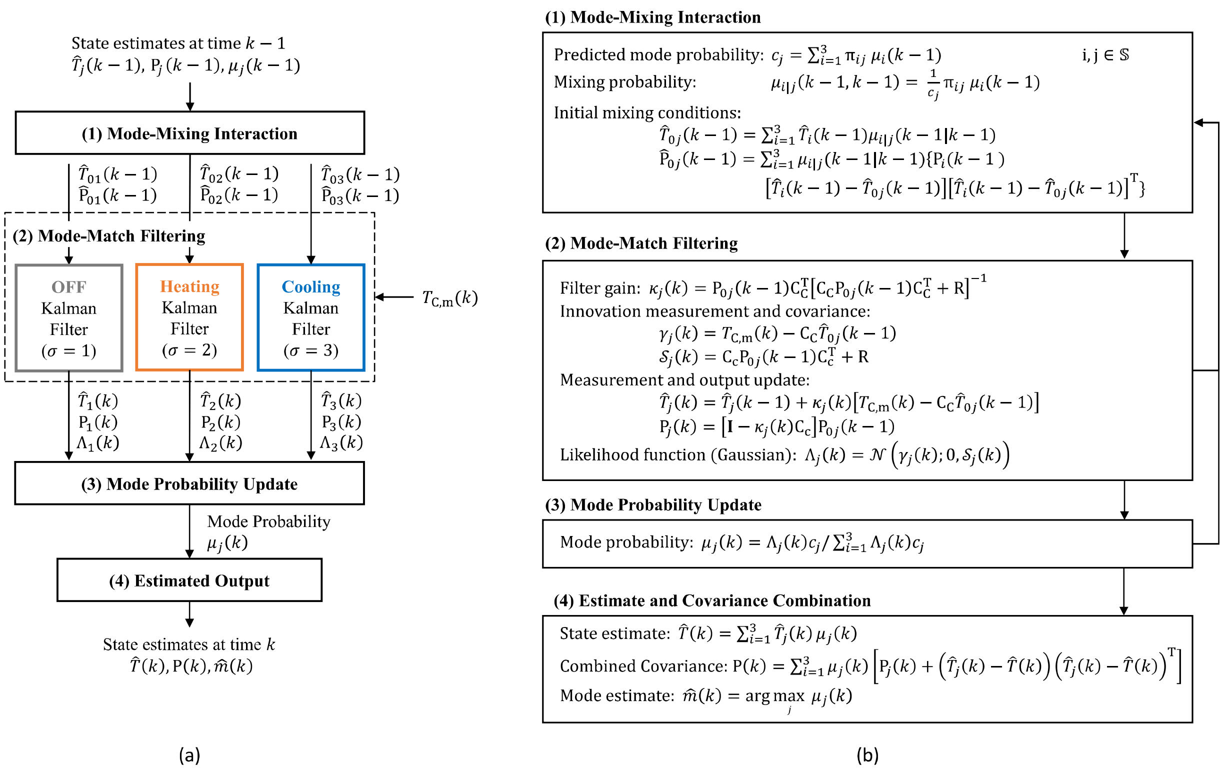

Fig. 4. Thermal transfer system IMM algorithm: (a) structure and (b) flow diagram.

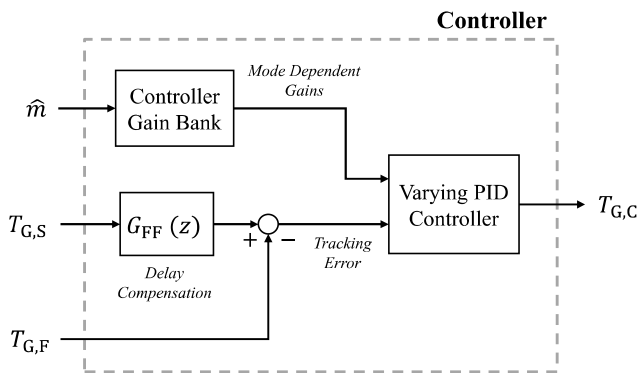

(a)

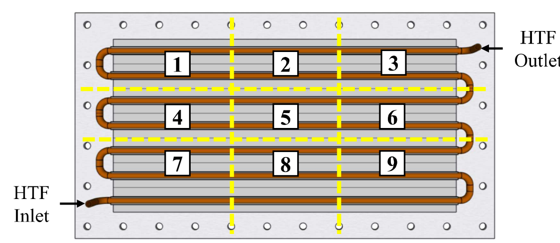

(b)

Fig. 5. Thermal transfer system components: (a) Controller block diagram, and; (b) thermal transfer panel feedback sensor layout.

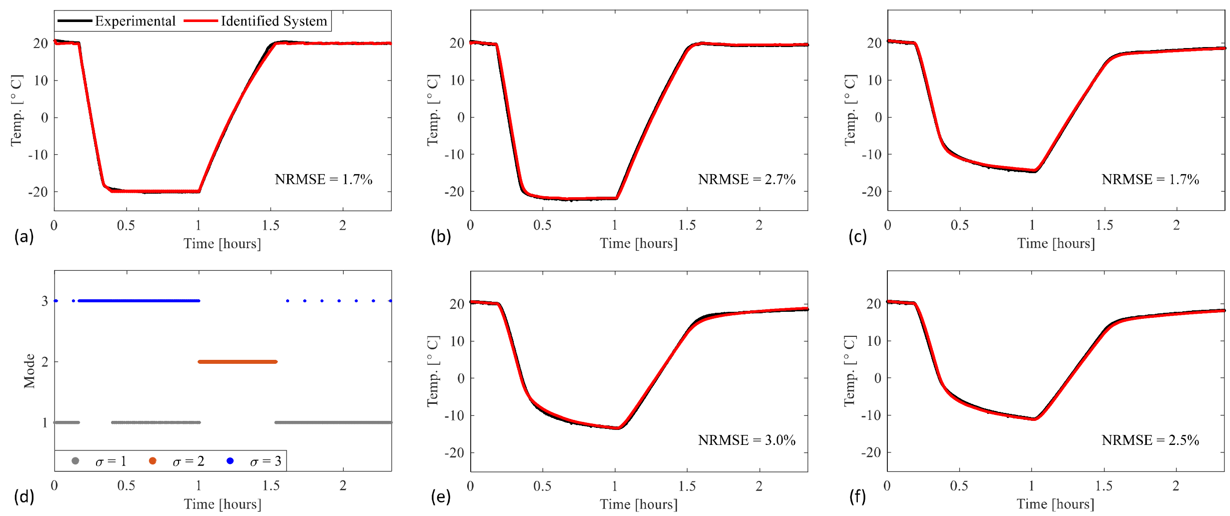

Fig. 6. Sample model validation test results (signal 4): (a) chiller; (b) thermal transfer pipe system; (c) thermal transfer in-panel area; (d) chiller mode determined by the model's control logic; (e) thermal transfer mid-panel area; (f) thermal transfer out-panel area.

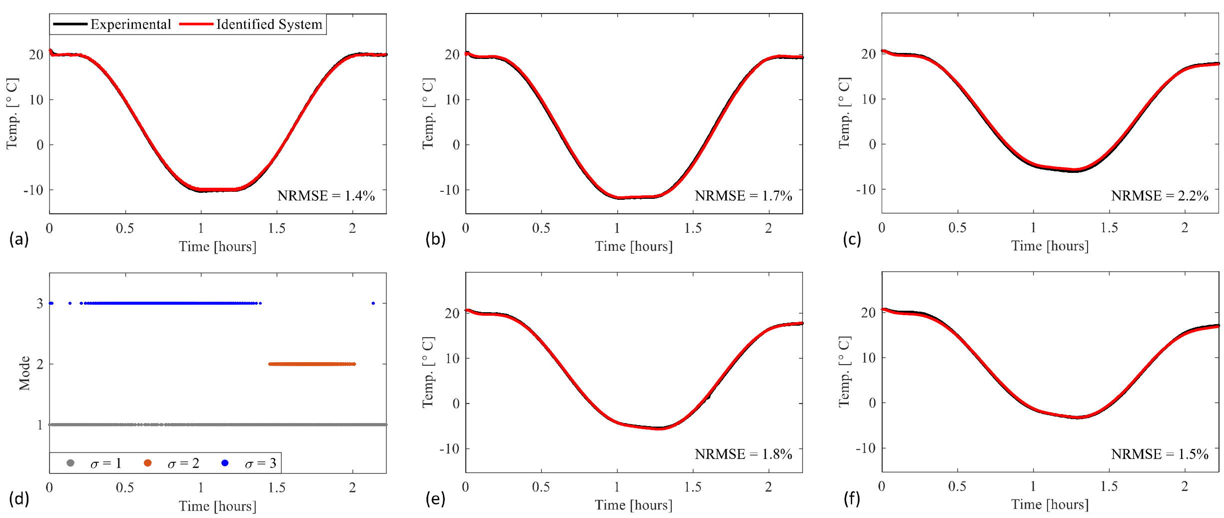

Fig. 7. Sample model validation test results (signal 10): (a) chiller; (b) thermal transfer pipe system; (c) thermal transfer in-panel area; (d) chiller mode determined by the model's control logic; (e) thermal transfer mid-panel area; (f) thermal transfer out-panel area.

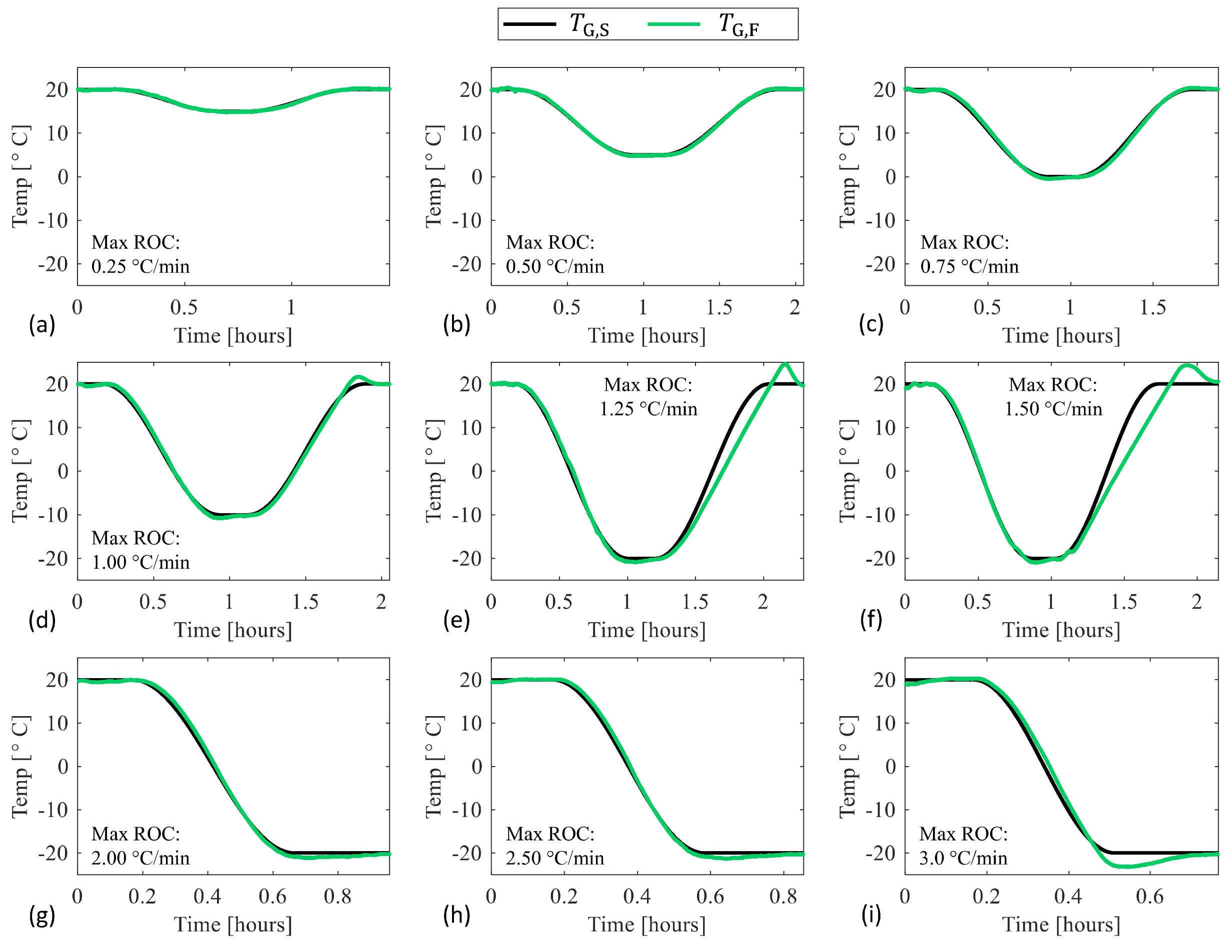

Fig. 8. Thermal transfer system control validation results: (a) Test 1; (b) Test 2; (c) Test 3; (d) Test 4; (e) Test 5; (f) Test 6; (g) Test 7; (h) Test 8; and (i) Test 10.

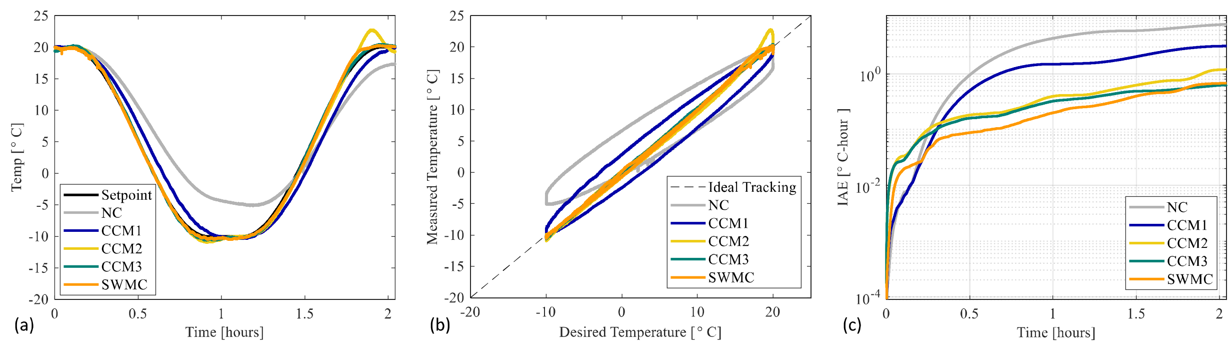

Fig. 9. Switching-mode controller comparison to other controllers: (a) time history; (b) tracking performance; and (c) IAE error.

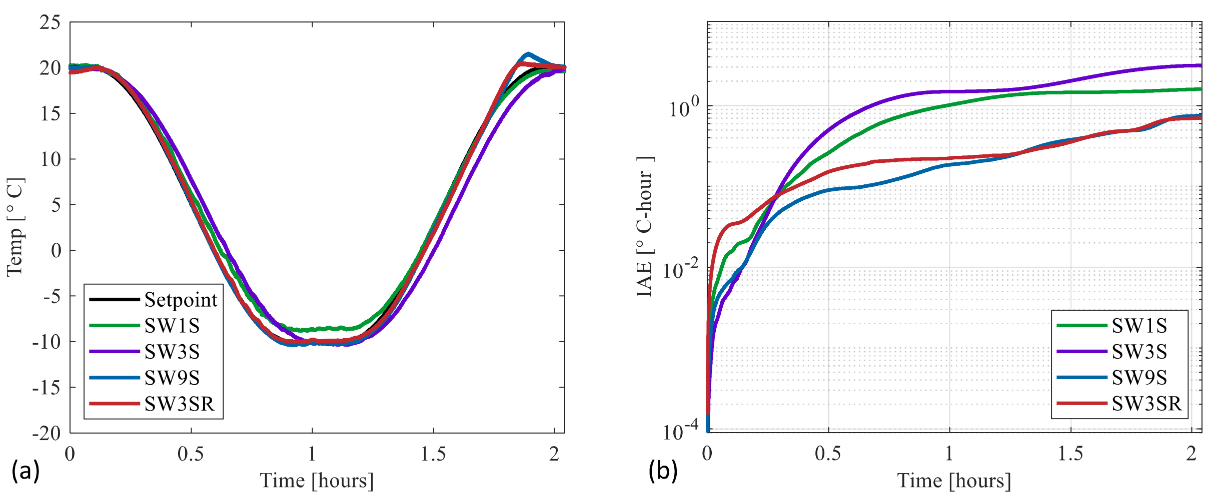

Fig. 10. Thermal transfer panel spatial temperature comparison by controller feedback scheme: (a) time history; and (b) IAE error.